Mapping nitrogen heteroatoms in carbon fibres using atom probe tomography and photoelectron spectroscopy

Carbon 179 (2021) 20–27

Contents lists available at ScienceDirect

Carbon

journal homepage: www.elsevier.com/locate/carbon

Mapping nitrogen heteroatoms in carbon fibres using atom probe tomography and photoelectron spectroscopy

Marcus Johansen [a, *], Christoph Schlueter [b], Pui Lam Tam [a], Leif E. Asp [a], Fang Liu [a, **]

[a] Department of Industrial and Materials Science, Chalmers University of Technology, SE-412 96, Gothenburg, Sweden
[b] Deutsches Elektronen-Synchrotron, D-22607, Hamburg, Germany

ARTICLE INFO

Article history:
Received 5 February 2021
Received in revised form
17 March 2021
Accepted 27 March 2021
Available online 1 April 2021

Keywords:
Carbon fibres
Multifunctional
Electrochemical
Atom probe tomography
Synchrotron
Hard X-ray photoelectron spectroscopy

ABSTRACT

Carbon fibres show great potential as multifunctional negative electrode for novel structural battery composites – a rechargeable electrochemical cell with structural function. The electrochemical performance of carbon materials can be enhanced with nitrogen heteroatoms, which conveniently are inherent in polyacrylonitrile (PAN)-based carbon fibres. However, it is not fully understood how the electrochemical performance is governed by microstructure and composition of the carbon fibres, particularly the distribution and chemical states of nitrogen heteroatoms. Here we reveal the atom-by-atom three-dimensional spatial distribution and the chemical states of nitrogen in three PAN-carbon fibre types (M60J, T800 and IMS65), using atom probe tomography (APT) and synchrotron hard X-ray photoelectron spectroscopy (HAXPES), and correlate the results to electrochemical performance. The findings pave the way for future tailoring of carbon fibre microstructure for multifunctional applications.

1. Introduction

Carbon fibres are among the best commercial materials in regard to specific strength and stiffness, providing superior reinforcement in lightweight composites for structural applications. Thanks to their capability to also reversibly intercalate ions during electrochemical processes, they are increasingly explored to realize many other functionalities, while simultaneously keep the structural function. One interesting example is the so-called structural battery composites, where besides as reinforcement, carbon fibres act as host for lithium (Li) ions, thereby storing electrochemical energy as negative electrode. This multifunctional device shows great potential to reduce the weight of electric vehicles and portable electronic devices [1–3]. Another example is morphing enabled by Li ion intercalation into carbon fibres, where large deformations and high actuation forces are realized at very low voltage [4].

The majority of carbon fibres are manufactured from the precursor polyacrylonitrile (PAN) with chemical formula $(C_3H_3N)_n$. During manufacture, PAN precursor fibres undergo multiple steps of thermal treatment that alter their chemical composition and structure. Depending on the treatment, the obtained carbon fibres contain from 90 to >99 wt% carbon (C), the rest being mainly oxygen (O) and nitrogen (N) [5,6]. Doping heteroatoms, in particular N, into carbon materials is a common method to enhance electrochemical properties [7–11]. For instance, N-doped graphene showed almost doubled reversible discharge capacity compared to pristine graphene [7]. Large increase in reversible discharge capacity was also reported in N-doped mesocarbon microbeads [8]. However, in order to achieve enhanced electrochemical performance, N-doping must be well controlled, since in carbon materials N heteroatoms can have different chemical states, and consequently different effects on active sites and conductivity [12–17]. It is worth noting that N are intrinsically abundant in the PAN precursor, hence it provides a convenient "in-situ" route to produce N-doped carbon fibres. Knowledge of the distribution and chemical states of heteroatoms in carbon fibres is essential for a fundamental understanding of their effects on electrochemical properties. However, such knowledge is still largely lacking.

Investigation of heteroatom distribution in carbon fibres requires analysis techniques with high spatial resolution, since during carbon fibre manufacturing the local differences in thermal and chemical conditions can lead to different local chemistry and

* Corresponding author.
** Corresponding author.
E-mail addresses: marcus.johansen@chalmers.se (M. Johansen), fang.liu@chalmers.se (F. Liu).

https://doi.org/10.1016/j.carbon.2021.03.061

microstructure [18]. Previously, N distribution in carbon fibres was investigated using transmission electron microscopy equipped with electron energy loss spectroscopy (EELS) [19]. Although the in-plane spatial resolution of EELS is high (in the lower nanometre range), all material information perpendicular to that plane is completely compressed into one point. Thus, information in three dimensions (3D) is collapsed into two dimensions. Atom probe tomography (APT) is a powerful technique that can map individual atoms in 3D with sub-nanometre resolution [20]. APT utilises a high local electric field (~10^{10} V/m), together with either voltage or laser pulses, to field evaporate atoms from a needle shaped specimen (end radius <50 nm) atom by atom, layer by layer. The time-of-flight of individual ions are measured to identify their species. Hit location of the ion is recorded by a position sensitive detector. Together with information on hit sequence, a 3D reconstruction can be obtained with the relative position and chemical species of each individual ion. APT has been extensively used for metallic materials. Only in recent years with the advent of laser pulsing, has APT been extended to analyse semi-conductors, oxides and even biomaterials [21-25]. Despite the ever-increasing application of APT to non-metallic materials, there have been only very few attempts to use APT to analyse carbon materials [26-30], and even fewer for carbon fibres [31,32]. To the best of our knowledge, no 3D atom map of carbon fibres was presented before.

The chemical states of atoms are routinely determined with X-ray photoelectron spectroscopy (XPS), but in the case of relatively low levels of N, lab-based XPS lacks the sensitivity and resolution for clear chemical state analysis. Instead, the required sensitivity can be provided with synchrotron-based hard X-ray photoelectron spectroscopy (HAXPES), thanks to tuneable X-ray radiation, with high flux and high energy resolution. Compared to XPS with incident X-ray energy ~1.3 keV and acquired information limited to the few top nanometres of a material, HAXPES utilises larger X-ray energies and thus determine chemical states at various greater depths [33].

Three types of commercial PAN-based carbon fibre, M60J (Toray), T800 (Toray) and IMS65 (Teijin) were investigated using APT and HAXPES. M60J is a high-modulus (HM) carbon fibre, and T800 and IMS65 are intermediate-modulus (IM) carbon fibres. Their microstructure, specifically crystal structure, and electrochemical performance were reported previously [34,35], which are summarised together with their physical properties in Table 1. It is worth noting that the capacity of the IM carbon fibres is comparable with the theoretical maximum capacity of graphite (372 mAh/g).

Here we present the distribution of N heteroatoms through 3D atom-by-atom reconstruction using APT and the chemical states of N at varying probe depths using HAXPES. We also correlate the results to the electrochemical performance of the carbon fibres. The new insights will enable us to design carbon fibres for multifunctional applications.

2. Materials and methods

2.1. Materials

Three types of PAN-based commercial carbon fibres were investigated: M60J, T800 and IMS65. The nominal diameter of all three fibre types is 5 μm. M60J and T800 were provided with sizing, which is routinely applied on the fibre surface by the manufacturer to improve adhesion to polymer matrices for composite manufacturing. IMS65 had no sizing.

2.2. Atom probe tomography

Atom probe tomography analyses were conducted in an IMAGO LEAP 3000X HR in pulsed laser mode. Its detector efficiency was 37% and image compression factor was 1.65. Wavelength of the laser was 532 nm. The laser pulse duration was 12 ps. The laser pulse frequency and energy were 100 kHz and 1 nJ, respectively. Specimen temperature was set to 100 K and acquisition rate to 2 ions per 1000 pulses. Premature failure is a big challenge for APT analysis of carbon related materials. All except two specimens were run until fracture. The radius of the two APT specimens before and after field evaporation were used to determine reconstruction parameters, since the field evaporation behaviour of turbostratic graphite is largely unknown. The software IVAS 3.4.3 (CAMECA) was used to reconstruct the obtained data.

Atom probe analysis requires specimens with sharp tips, radius <50 nm, in order to generate sufficiently high electric fields that can ionise surface atoms. In order to fabricate nano-tips from carbon fibres, in-situ lift out [38] was performed in a FEI Versa 3D workstation, a combined focused ion beam and scanning electron microscope (FIB/SEM). The FIB uses gallium (Ga) ions to sputter away material and the SEM allows for real-time monitoring of the process. The FIB/SEM is equipped with an Omniprobe system for micro-manipulation, and a platinum (Pt) gas injection system, which can be used for electron induced chemical vapour deposition of Pt.

Before being placed in the FIB/SEM, a single fibre was isolated and adhered with silver glue to a silicon (Si) wafer. The fibre was positioned in either of two ways, laterally – the carbon fibre simply lies on the wafer (Fig. 1a), or cross-sectionally – the carbon fibre sticks out of the edge of a vertically placed wafer (Fig. 1b). The different positioning allows extraction of specimens either close to the fibre surface or close to the fibre centre.

In the FIB/SEM, a region of interest was first coated with Pt to protect the material from Ga implantation. Trenches were milled along the region of interest to produce a wedge of carbon fibre (~15 μm long for the lateral surface, and ~5 μm for cross-sectional surface), which was adhered to the Omniprobe needle using Pt and then extracted (Fig. 1c). The free end of the wedge was adhered to one of the pre-manufactured Si micro posts (CAMECA) using Pt,

Table 1
Physical properties, crystal structure and electrochemical performance of M60J, T800 and IMS65 retrieved from Ref. [34]* [35],** [36], and [37].

	M60J	T800	IMS65
Final heat treatment temperature range (°C)	1800–3000	1100–1600	1100–1600
Tensile modulus (GPa)	588	294	290
Tensile strength (MPa)	3920	5490	6000
Electrical resistivity (Ω·cm × 10^{-3})	0.7	1.4	1.45
Thermal conductivity (cal/(cm·s·K))	0.363	0.0839	–
Average crystal length (Å)*	>300	18	19
Average crystal thickness (Å)*	>100	18	28
Interlayer spacing (002) (Å)*	3.47	3.70	3.49
1st cycle capacity (mAh/g)**	159	265	358
10th cycle capacity (mAh/g)**	154	243	317

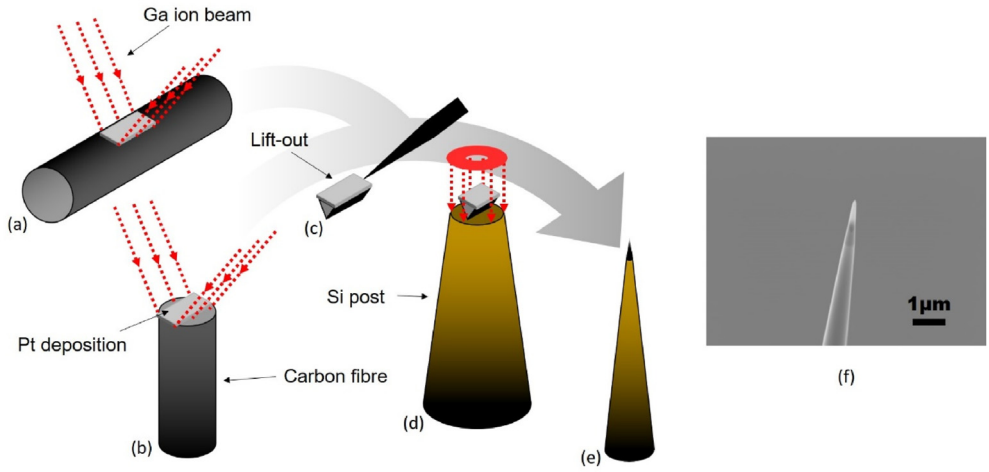

Fig. 1. Schematic of carbon fibre specimen fabrication for APT. A protective Pt layer is deposited on (a) the lateral or (b) the cross-sectional fibre surface; and the Ga ion beam mills a wedge shape close to the Pt layer. (c) The wedge of carbon fibre is cut free and extracted using the micro-manipulator. (d) Part of the wedge is adhered with Pt to a Si post, cut free, and annularly milled to (e) a sharp tip. (f) A SEM image of a sharpened APT tip of carbon fibre. (A colour version of this figure can be viewed online.)

and then cut free from the rest. This process was repeated until the wedge had been consumed. Thus 2–5 APT tips were obtained for each lift-out. To ensure better adhesion, the stage was rotated 180° and Pt was deposited on the other side of the posts as well. Then the material piece was ion milled with an annular ring pattern (Fig. 1d) into nano-tips (Fig. 1e and f): first at 30 kV accelerating voltage with a series of ion currents from 500 to 100 pA, and finally, at 2 kV to mitigate ion beam damage to the material. It should be noted, although FIB is known to introduce various artefacts, such as surface amorphization and Ga implantation, into the material, based on our previous studies of carbides and nitrides in steels [39] and Ti(C,N) in cubic BN [40], it is unlikely to activate N diffusion, particularly underneath the surface. Thus, the initial distribution of N is maintained.

Since FIB milling can easily remove any sizing (~100 nm thick) from the surface, for APT specimen preparation all fibres were used in their as-received state without sizing removal. APT results show no evidence of remaining sizing.

2.3. X-ray photoelectron spectroscopy

A PHI 5500 Multi-technique System was used for lab-based XPS. Due to the less conductive nature of the samples, Mg Kα X-ray source was used (1253.6 eV) to avoid the need for charge compensation procedure during measurements.

HAXPES was performed at the P22 beamline at PETRA III (DESY Hamburg, Germany) [41]. Spectra were recorded at incident X-ray energies 2.5, 4.6 and 7.2 keV for all three fibre types. Several scans were made for each fibre type and multiple sweeps were made for each scan. The carbon fibres were assumed to only consist of C, N and O, so that after background removal and intensity correction, the relative intensities of C1s, N1s and O1s high resolution scans were proportional to the relative element concentration. Shirley type background removal was performed using MultiPak 9.7.0.1 and intensity correction was based on photoionisation cross-sections calculated for C1s, N1s and O1s according to Ref. [42] for 2.5, 4.6 and 7.2 keV (Table S1). No X-ray irradiation damage was detected. Repeated measurements at the same spot show no change in spectral line shape.

The projected X-ray beam size on the sample was approximately 800 μm for lab-based XPS and 100 μm for HAXPES, which are much larger than the carbon fibre diameter of 5 μm. Therefore, for each fibre type, a spread-out tow of multiple of fibres was analysed.

The sizing was removed from M60J and T800 prior to XPS and HAXPES measurements. Each tow of fibres was first submerged in acetone solvent in the 50 °C ultrasonic bath for an hour, and then rinsed with isopropanol three times to remove the residual acetone solvent. IMS65 fibres were also rinsed with isopropanol. Afterwards, all fibres were baked at 70 °C in low vacuum condition of 40 mbar for 3.5 h by using a Heraeus UT5050E oven to vaporise the residual moisture.

3. Results and discussion

3.1. Atom probe tomography

APT provides straightforward chemical quantification by direct ion counting from the mass-to-charge spectra. However, APT spectra of carbon fibres are complex, showing nearly one hundred mass-to-charge peaks (Fig. S1), consisting of monatomic ions and a multitude of molecular ions (ions that consist of at least two atoms) with overlapped ionic species. It is a big challenge to deconvolute the overlapping peaks and unambiguously assign each mass-to-charge peak to the corresponding ion species. Therefore, we started with unravelling the spectra of the HM carbon fibre, M60J, because it contains almost pure C with trace amount of O; besides, it exhibits better mass resolution than the IM carbon fibres, due to its higher thermal conductivity (four times higher) (Table 1). For laser pulsing APT, the thermal conductivity of the specimen plays a big role in determining the mass resolution [43]. All the peaks are identified, and deconvoluted, based on the natural abundance of the isotopes ^{12}C and ^{13}C, which gives a unique satellite peak and a theoretical ratio between peak areas of the isotope-pair $^{12}C_x^{n+}$ and $^{12}C_{(x-1)}^{13}C^{n+}$ (Fig. S2). At 28 and 44 Da, the significant deviation in the measured peak area ratio to the theoretical ratio is attributed to peak overlap with O-containing species, CO^{1+} and CO_2^{1+} (Fig. S3).

For the HM carbon fibre, the peaks associate predominantly with various combinations of C/C atoms and occasionally with combinations of C/O; and for the IM carbon fibres there are additional peaks associated with C/N. In all cases, the most abundant ions are monatomic carbon, C^{1+} and C^{2+}: for HM fibres 75–80% out of the total number of ions and for IM fibres 60–70%; most of the other peaks corresponds to molecular ions that consists of only carbons ($C_{2\text{-}22}^{1+/2+/3+/4+/5+}$). O was only detected in molecular ions

with other elements, such as $CO^{1+/2+}$, and CO_2^{1+}. The lack of pure O ions indicates high affinity of O to other elements. The O content varies between the fibres and even between different positions in the same fibre: 0.33–0.68 at% for M60J; 0.22–0.96 at% for T800; and 0.36–0.60 at% for IMS65. The major difference between the mass spectra obtained from HM and IM fibres is that the IM fibres have a much higher peak at 14 Da and several additional peaks at 7, 26, 27, 31, 38, 50, 62, 74 and 86 Da (Fig. 2 shows selected ranges between 6.5 and 31.5 Da). These peaks are unambiguously assigned as N containing: N^{2+}, CN^{1+}, C_2NO^{2+}, C_4N^{2+}, C_2N^{1+}, C_3N^{1+}, C_4N^{1+}, C_5N^{1+} and C_6N^{1+}. The peak at 14 Da can possibly be assigned as CH_2^{1+}, CO^{2+}, and/or N^{1+}. Since the peak was not evidently shown in polymers that contain CH_2 units [44], this peak corresponds most likely to CO^{2+} for the HM fibre, and a mix of primarily N^{1+} and traces of CO^{2+} for the IM fibres.

Before discussing the distribution of N in the IM fibres, it is important to note the analysis volume of APT and where the volume of material located originally in the carbon fibre. APT boasts atomic spatial resolution for chemical analysis. However, as for all the techniques with high spatial resolution, the analysis volume of APT is limited. Particularly for carbon fibres, the combination of strong covalent bonds within the graphene layer and weak Van der Waals force between layers, together with a large number of nano pores, leads to frequent premature specimen fracture and the analysis length is often limited to less than 50 nm. Furthermore, due to the manual control during the needle shaping procedure, the removed amount of material varies slightly between specimens. Therefore, the tip of each specimen corresponds to different depths below the carbon fibre surface – up to tens of nanometres in difference. Finally, the sites of the APT analysis volumes in the carbon fibre can be selected: we extracted specimens from different depths with either the lateral or cross-sectional geometry.

3D atom-by-atom reconstructions of obtained APT datasets from IM fibres show that the N distribution is smooth and there is no distinct agglomeration of N (Fig. 3a, Fig. S4 and Video S1). For the near surface region (from lateral specimen preparation), the average N concentration varies between the APT specimens: T800 1.6–2.9 at% and IMS65 1.3–2.9 at% (Table S2). Fig. 3b and c show the typical N concentration profiles along the analysis axis, i.e. from near the surface towards the centre of the fibre, for T800 and IMS65. The N content generally increases with depth within the analysis volume. However, the rate of N concentration increase (around ~0.2 at% per 10 nm) cannot be constant over the ~2500 nm to the fibre core, since the APT specimens extracted from the cross-section (500–2500 nm in depth) have an average N concentration of 2.4–3.5 at% for T800 (Table S2). The APT results thus indicate that the N distribution varies smoothly in small domains, but the distribution is uneven on the long range over the IM fibres.

Supplementary video related to this article can be found at https://doi.org/10.1016/j.carbon.2021.03.061

3.2. Hard X-ray photoelectron spectroscopy

In order to shed light on the chemical states of N, we analysed the fibres using photoelectron spectroscopy, including both lab-based XPS and synchrotron HAXPES. Compared with lab-based XPS, synchrotron HAXPES provides more information from the bulk. The probe depth is correlated to the energy of incident X-rays. For lab-based XPS, the photon energy is ~1.3 keV, and the detection depth is less than 10 nm. 95% of the detected signal originates from within the depth of 3.0 times the inelastic mean free path (IMFP) [45]. For HAXPES, at excitation energies of 2.5, 4.6 and 7.2 keV used in our study and IMFP approximated according to Ref. [46], the probe depth in graphitic materials is estimated to be 17, 28 and 40 nm, respectively. HAXPES survey scan spectra of the carbon fibres show C1s, N1s and O1s at around 285 eV, 400 eV and 532 eV, respectively (Fig. 4a), whereas lab-based XPS hardly detects N1s (Fig. S5).

The most distinct difference between the carbon fibres is found at the N1s region. The IM fibres generate pronounced N1s peaks, while the HM fibre gives a very weak signal that is only distinguishable in scans with higher resolution (Fig. 4a insert). Quantification of data obtained at different energies show that the relative composition varies for different depths (Fig. 4b and c). The O content decreases rapidly with depth for all fibre types: 3.7 at% for the first 17 nm and 1.7 at% for the entire 40 nm region for M60J, 5.6 at% for the first 17 nm and 2.0 at% for 40 nm region for T800, and 6.7 at% for the first 17 nm to 2.8 at% for 40 nm region for IMS65. The N content varies differently between the fibre types: M60J and IMS65 decreases; and T800 increases. At the highest X-ray energy, the N content is 1.5 at% for IMS65, 1.2 at% for T800 and 0.1 at% for M60J.

Thus, the HAXPES results are consistent with APT in the aspect that the N content is significantly higher in IM fibres. However, HAXPES unambiguously detects traces of N in the HM fibres, while APT does not. Additionally, the N concentration profiles against the depth are different: APT showed a generally increase trend for both IMS65 and T800, while HAXPES showed increase for T800 and decrease for IMS65. This discrepancy in N detection between APT

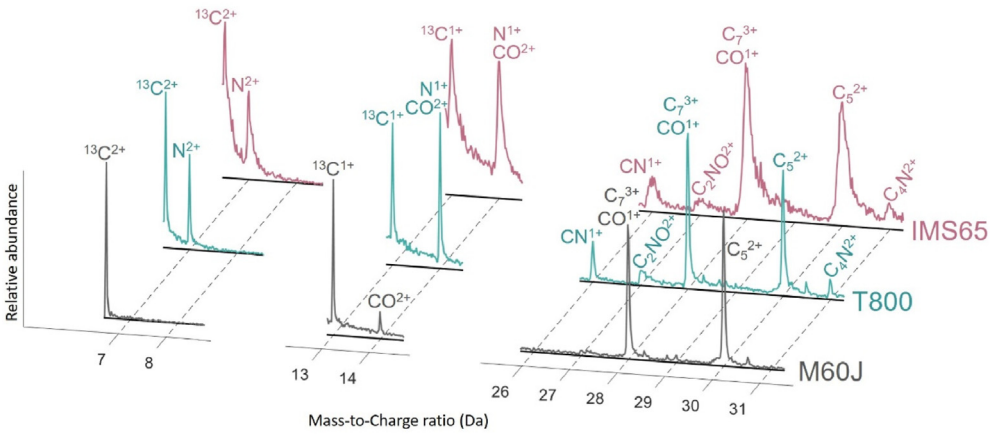

Fig. 2. Comparison of selected ranges of mass-to-charge spectra for HM carbon fibre, M60J, and IM carbon fibres, T800 and IMS65. Note the absence of N-containing species in the spectrum for M60J compared to T800 and IMS65. Note that since there is big difference in the peak height, the peaks are scaled separately in each range. (A colour version of this figure can be viewed online.)

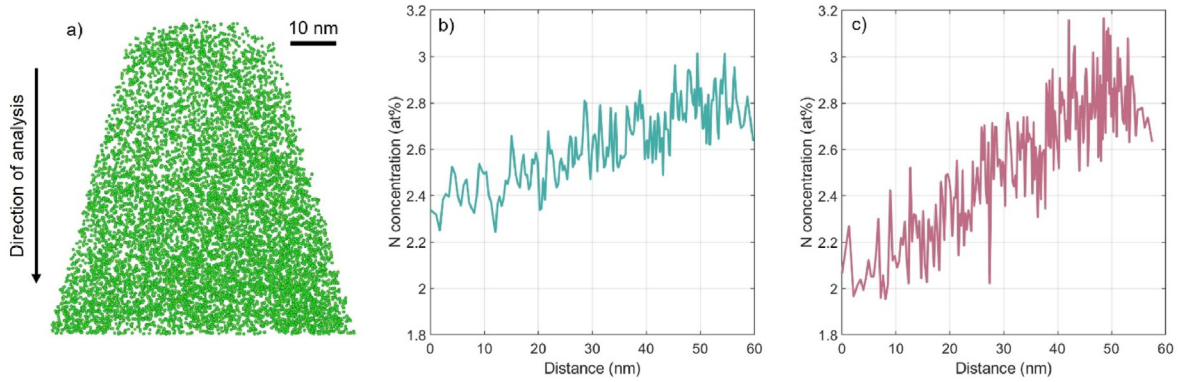

Fig. 3. (a) 3D atom-by-atom reconstruction of N atoms in T800. For clarity's sake, only 10% of the acquired N atoms are shown. N concentration profile of lateral specimens of (b) T800 and (c) IMS65. (A colour version of this figure can be viewed online.)

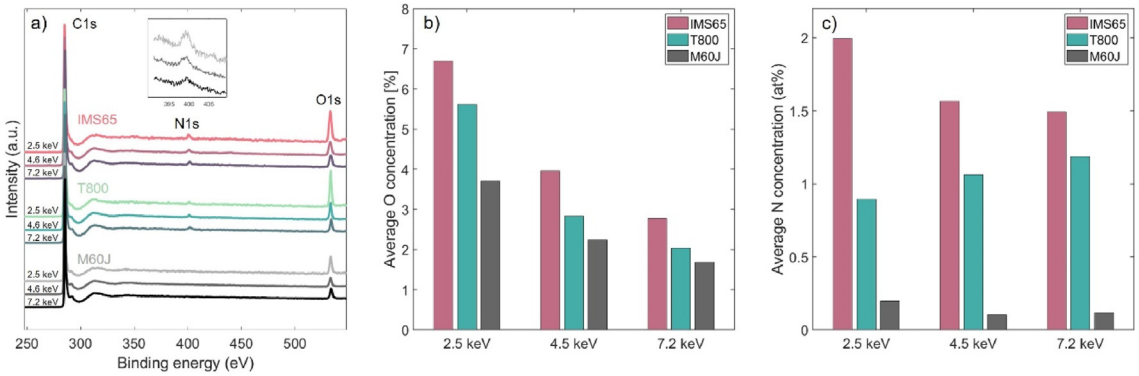

Fig. 4. (a) HAXPES survey scan spectra of M60J, T800 and IMS65 for three incident energies, with inset of high resolution N1s narrow scan spectra of M60J, where the peak is small but clear. (b) O and (c) N concentration for different incident energies for M60J, T800 and IMS65. (A colour version of this figure can be viewed online.)

and HAXPES can be explained by several factors: in APT the possible peak overlap at 14 Da can overshadow the N signals; HAXPES analyses cover a much larger area consisting of tens of carbon fibres, whereas APT probes at the nanometre scale; additionally, HAXPES analysis volumes are close to the surface, while in our studies APT often probe deeper into carbon fibres. Thus, it is implausible to directly compare the quantification results of APT and HAXPES.

The chemical states of N are revealed by deconvoluting the N1s peak of the IM fibres. Five N species are used to fit N1s peaks for IMS65 (Fig. 5a–c) and T800 (Fig. 5e–g): pyridinic-N at 398.5 eV, pyrrolic-N at 399.6 eV, graphitic-N at 401.0 eV, edge-located graphitic-N at 402.2 and oxidic-N at 403.8 eV. Pyridinic-N (N1 in Fig. 5i) is bonded to two carbon atoms of a six-membered ring at an edge or a defect in the hexagonal carbon lattice. Pyrrolic-N (N2 in Fig. 5i) is bonded in a five-membered ring. Graphitic-N (N3 in Fig. 5i) substitutes a carbon atom in the graphene plane; edge-located graphitic-N (N4 in Fig. 5i) substitutes a carbon atom at the edge of the plane; and thereby both types are bonded to three carbon atoms. Oxidic-N (N5 in Fig. 5i) is bonded to two carbon atoms and one oxygen atom [47–50]. The content of the N species is different in IMS65 and T800, varying with depth (Fig. 5d and h). While the pyridinic-N peak decreases in IMS65 (8.6%, 7.8%, 4.6% out of the total N species for the layer with thickness of 17, 28 and 40 nm, respectively), it increases in T800 (2.6%, 5.1%, 5.6%). At the same time the level of pyrrolic-N decreases for both IMS65 (24.7%, 19.3%, 15.9%) and T800 (17.3%, 10.6%, 8.6%). The most abundant N species in both cases is graphitic-N, and the level is lower in IMS65 (47.7%, 50.6%, 53.6%) than T800 (53.6%, 55.6% and 59.6%). Thus, for both IM fibres the deeper into the fibres, the higher amount of graphitic-N. The HAXPES results show that the chemical states of N in carbon fibres differ between IM fibres and vary with depth.

3.3. *Effect of heteroatoms on electrochemical performance*

IM fibres (IMS65 and T800) have superior electrochemical properties compared to HM fibres (M60J): their first cycle capacity is 358 and 265 vs 159 mAh/g [35]. The difference in electrochemical performance was previously attributed to the size and orientation of crystallites in IM and HM carbon fibres [34]. In this study, the APT and HAXPES results show that the presence of N is another essential aspect that sets IM and HM fibres apart. N is an inherent component of the PAN precursor $(C_3H_3N)_n$. During manufacture, the precursor fibres undergo at least two heat treatment steps that change the chemical make-up of the fibres: firstly, oxidisation in air, where O is introduced to form stable ladder structure for later steps at higher temperature; secondly, carbonisation in inert gas, where most non-carbon atoms are removed from the fibre and a turbostratic structure is obtained; optionally, if high modulus is sought, graphitisation in inert gas, where the structure becomes more ordered and even more non-carbon atoms are expelled. The heat treatment, and specifically the final heat treatment temperature, dictates the atomic composition, particularly N-content, strength and modulus of carbon fibres [5,6]. Compared to IM fibres, HM carbon fibres are heat treated at a higher temperature, thus more heteroatoms like N are removed, and more crystalline structure are obtained, yielding a higher modulus. The IM fibres contain up to

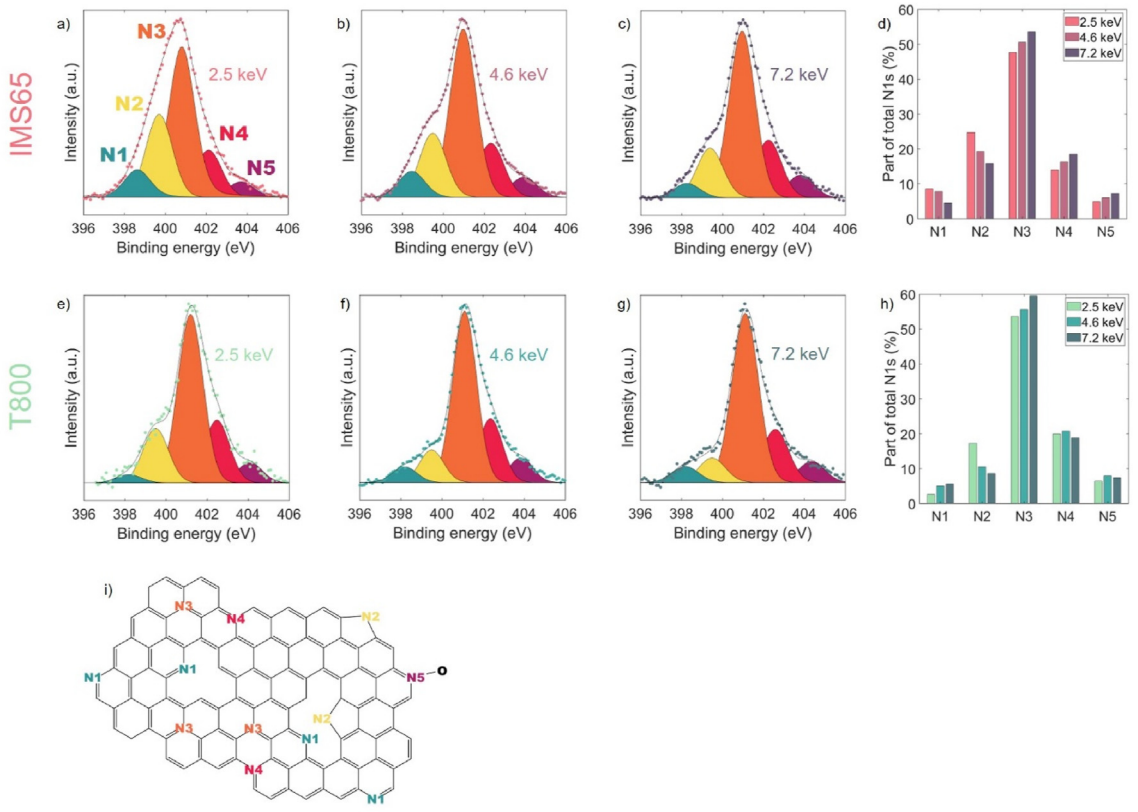

Fig. 5. Deconvolution of N1s peaks from HAXPES of IMS65 and T800. The N species are denoted N1 for pyridinic-N, N2 for pyrrolic-N, N3 for graphitic-N, N4 for edge-located graphitic-N and N5 for oxidic-N. The top row is IMS65 at increasing incident energy (a) 2.5 keV, (b) 4.6 keV and (c) 7.2 keV. (d) The composition of N species in IMS65 at different sub-surface volumes. The bottom row is T800 at (e) 2.5 keV, (f) 4.6 keV and (g) 7.2 keV. (h) The composition of N species in IMS65 at different sub-surface volumes. (i) A schematic of possible N configurations in carbon. (A colour version of this figure can be viewed online.)

3.5 at% N, whereas the HM fibre contain virtually none. It is well established that doping N heteroatoms into carbon materials positively affect the electrochemical properties of the materials [7,10,12–15]. Thus, the N heteroatoms in the IM fibres are linked to their enhanced electrochemical performance compared to HM fibres.

Still, for the two IM fibres, with similar level of N concentration, their electrochemical performance differs significantly: the capacity of IMS65 is more than one third higher than that of T800. It was previously shown that the sizing applied to the surface of T800 did not impair electrochemical performance [35]. Neither can the difference be explained by the crystallite size, since IMS65 and T800 are very similar in this regard [34]. The higher oxygen concentration for IMS65 measured with HAXPES may potentially influence the electrochemical performance. However, there is little evidence in literature of such mechanism. The difference stems most likely from N configurations. Graphitic-N is predominant in both IM fibres (>50%). It has a n-type doping effect by donating electrons to the system [16], thus favourable for the electronic conductivity, which enables, for instance, fast charge and discharge. However, IMS65 has less N configured as graphitic-N than T800, but shows better electrochemical performance, which suggests that the n-type doping effect from graphitic-N is not responsible for the significant increase in electrochemical performance. Moreover, it has been shown that n-type doping effect can be cancelled out by the p-type doping effect of pyridinic-N and pyrrolic-N [17]. On the other hand, it has been shown theoretically and experimentally that pyridinic-N and pyrrolic-N boost electrochemical performance of carbon materials by inducing defects (edges and vacancies) in the graphene lattice, which act as active sites for Li adsorption [11–15]. In IMS65, a higher level of N has the pyridinic- and pyrrolic-N configuration (~20% in total) compared to T800 (~14%). With comparable N concentration, IMS65 thus has more N induced defects working as active sites and consequently higher capacity than T800.

3.4. Future perspective

In this study, APT and HAXPES were used to elucidate heteroatoms in carbon fibres and their influence on electrochemical properties. There are still challenges to overcome. There were high rates of pre-mature specimen failures during APT analyses. This is largely attributed to the inherent anisotropic structure of carbon fibres with many defects, e.g. nano pores, together with the high evaporation field of graphite carbon. To coat the APT specimen with a thin layer of proper metal can be a promising solution. With more successful and longer analyses, other interesting features can potentially be revealed, for instance, the transitional areas between N-rich and N-poor regions. Synchrotron HAXPES provided chemical states of N in the “surface bulk”, up to 40 nm deep. To study N configuration at greater depths in the carbon fibres is highly desirable but requires sophisticated specimen preparation. In addition, how the local microstructure of carbon fibres influences the intercalation of Li ions is the subject of our ongoing work. For future perspective, linking the distribution and chemical states of heteroatoms with processing parameters of carbon fibres (e.g. temperature and environment) will enable the design of novel carbon fibres for multifunctional applications.

4. Conclusion

In this paper, we shed light on the heteroatoms, in particular N, in three fibre types (M60J, T800 and IMS65) with different capacity (159, 265 and 358 mAh/g), using APT and HAXPES. With the two strategies for specimen preparation (lateral and cross-sectional), we used APT to probe the local N concentration variation at different depths. It is shown that the HM fibre (M60J) contains close to zero N, whereas the IM fibres (T800 and IMS65) contain 1.3–3.5 at% N. The N distribution is non-homogenous on the large scale throughout the IM fibres. The chemical states of N vary within the IM fibres. In the top 40 nm of the turbostratic structure, graphitic-N becomes increasingly abundant with depth. IMS65 has a larger portion of pyridinic-N and pyrrolic-N (20.5%) than T800 (14.2%), which is, at least partly, responsible for the higher capacity of IMS65. These findings highlight the important role of N for the electrochemical performance of carbon fibres for multifunctional devices.

CRediT authorship contribution statement

Marcus Johansen: Methodology, Software, Validation, Formal analysis, Investigation, Data curation, Writing – original draft, Visualization. **Christoph Schlueter:** Methodology, Investigation, Resources, Writing – review & editing. **Pui Lam Tam:** Investigation, Resources, Writing – review & editing. **Leif E. Asp:** Conceptualization, Resources, Writing – review & editing. **Fang Liu:** Conceptualization, Methodology, Validation, Investigation, Writing – original draft, Supervision, Project administration, Funding acquisition.

Declaration of competing interest

The authors declare that they have no known competing financial interests or personal relationships that could have appeared to influence the work reported in this paper.

Acknowledgement

This work was financially supported by the Swedish Energy Agency (Project nr 46598-1). FL and LA thank the strategic innovation program LIGHTer (funding provided by Vinnova, the Swedish Energy Agency and Formas). We acknowledge DESY (Hamburg, Germany), a member of the Helmholtz Association (HGF) and the Federal Ministry of Education and Research (BMBF) for the provision of HAXPES instrumentation at beamline P22.

Appendix A. Supplementary data

Supplementary data to this article can be found online at https://doi.org/10.1016/j.carbon.2021.03.061.

References

[1] L.E. Asp, M. Johansson, G. Lindbergh, J. Xu, D. Zenkert, Structural battery composites: a review, Funct. Compos. Struct. 1 (4) (2019), 042001.
[2] W. Johannisson, D. Zenkert, G. Lindbergh, Model of a structural battery and its potential for system level mass savings, Multifunct. Mater. 2 (3) (2019).
[3] L.E. Asp, K. Bouton, D. Carlstedt, S. Duan, R. Harnden, W. Johannisson, M. Johansen, M.K.G. Johansson, G. Lindbergh, F. Liu, K. Peuvot, L.M. Schneider, J. Xu, D. Zenkert, A structural battery and its multifunctional performance, Adv. Energy Sustain. Res. 2 (2021) 2000093. https://doi.org/10.1002/aesr.202000093.
[4] W. Johannisson, R. Harnden, D. Zenkert, G. Lindbergh, Shape-morphing carbon fiber composite using electrochemical actuation, Proc. Natl. Acad. Sci. U. S. A 117 (14) (2020) 7658–7664.
[5] X. Huang, Fabrication and properties of carbon fibers, Materials 2 (4) (2009) 2369–2403.
[6] M.L. Minus, S. Kumar, The processing, properties, and structure of carbon fibers, JOM (J. Occup. Med.) 57 (2) (2005) 52–58.
[7] A.L.M. Reddy, A. Srivastava, S.R. Gowda, H. Gullapalli, M. Dubey, P.M. Ajayan, Synthesis of nitrogen-doped graphene films for lithium battery application, ACS Nano 4 (11) (2010) 6337–6342.
[8] P. Han, et al., Nitrogen-doping of chemically reduced mesocarbon microbead oxide for the improved performance of lithium ion batteries, Carbon N. Y. 50 (3) (2012) 1355–1362.
[9] Z. Xing, et al., One-pot hydrothermal synthesis of Nitrogen-doped graphene as high-performance anode materials for lithium ion batteries, Sci. Rep. 6 (April) (2016) 1–10.
[10] M. Inagaki, M. Toyoda, Y. Soneda, T. Morishita, Nitrogen-doped carbon materials, Carbon N. Y. 132 (2018) 104–140.
[11] Z. He, et al., Electrospun nitrogen-doped carbon nanofiber as negative electrode for vanadium redox flow battery, Appl. Surf. Sci. 469 (2018) 423–430, 2019.
[12] X. Wang, et al., Atomistic origins of high rate capability and capacity of N-doped graphene for lithium storage, Nano Lett. 14 (3) (2014) 1164–1171.
[13] F. Zheng, Y. Yang, Q. Chen, High lithium anodic performance of highly nitrogen-doped porous carbon prepared from a metal-organic framework, Nat. Commun. 5 (May) (2014) 1–10.
[14] B. Zhang, et al., Correlation between atomic structure and electrochemical performance of anodes made from electrospun carbon nanofiber films, Adv. Energy Mater. 4 (7) (2014).
[15] Y.F. Li, Z. Zhou, L.B. Wang, CNx nanotubes with pyridine like structures: p-type semiconductors and Li storage materials, J. Chem. Phys. 129 (10) (2008).
[16] T. Schiros, et al., Connecting dopant bond type with electronic structure in n-doped graphene, Nano Lett. 12 (8) (2012) 4025–4031.
[17] D. Usachov, et al., The chemistry of imperfections in N-graphene, Nano Lett. 14 (9) (2014) 4982–4988.
[18] H. Khayyam, et al., PAN precursor fabrication, applications and thermal stabilization process in carbon fiber production: experimental and mathematical modelling, Progress in Materials Science 107 (2020) 100575.
[19] V. Serin, R. Fourmeaux, Y. Kihn, J. Sevely, M. Guigon, Nitrogen distribution in high tensile strength carbon fibres, Carbon N. Y. 28 (4) (1990) 573–578.
[20] T.F. Kelly, M.K. Miller, Atom probe tomography, Rev. Sci. Instrum. 78 (3) (2007).
[21] T.J. Prosa, S.K. Keeney, T.F. Kelly, Atom probe tomography analysis of poly(3-alkylthiophene)s, J. Microsc. 237 (2) (2010) 155–167.
[22] L.M. Gordon, D. Joester, Nanoscale chemical tomography of buried organic-inorganic interfaces in the chiton tooth, Nature 469 (7329) (2011) 194–198.
[23] L.M. Gordon, L. Tran, D. Joester, Atom probe tomography of apatites and bone-type mineralized tissues, ACS Nano 6 (12) (2012) 10667–10675.
[24] P.R. Heck, et al., Atom-probe analyses of nanodiamonds from Allende, Meteoritics Planet Sci. 49 (3) (2014) 453–467.
[25] B. Langelier, X. Wang, K. Grandfield, Atomic scale chemical tomography of human bone, Sci. Rep. 7 (2017) 1–9. (Accessed November 2016).
[26] C. Ngo, M.A. Fitzgerald, M.J. Dzara, M.B. Strand, D.R. Diercks, S. Pylypenko, 3D atomic understanding of functionalized carbon nanostructures for energy applications, ACS Appl. Nano Mater. 3 (2) (2020) 1600–1611.
[27] K. Jiang, et al., Transition-metal single atoms in a graphene shell as active centers for highly efficient artificial photosynthesis, Inside Chem. 3 (6) (2017) 950–960.
[28] J.B. Lewis, D. Isheim, C. Floss, D.N. Seidman, 12C/13C-ratio determination in nanodiamonds by atom-probe tomography, Ultramicroscopy 159 (2015) 248–254.
[29] M. Raghuwanshi, O. Cojocaru-Mirédin, M. Wuttig, Investigating bond rupture in resonantly bonded solids by field evaporation of carbon nanotubes, Nano Lett. 20 (1) (2020) 116–121.
[30] S. Mukherjee, H. Watanabe, D. Isheim, D.N. Seidman, O. Moutanabbir, Laser-assisted field evaporation and three-dimensional atom-by-atom mapping of diamond isotopic homojunctions, Nano Lett. 16 (2) (2016) 1335–1344.
[31] O. Nishikawa, M. Taniguchi, Atomic level analysis of carbon fibers by the scanning atom probe, Surf. Interface Anal. 46 (12–13) (2014) 1231–1235.
[32] R.K.W. Marceau, et al., Local electrode atom probe tomography of carbon fibre, Microsc. Microanal. 25 (S2) (2019) 2496–2497.
[33] Hard X-Ray Photoelectron Spectroscopy (HAXPES), vol. 59, Springer International Publishing, Cham, 2016.
[34] G. Fredi, et al., Graphitic microstructure and performance of carbon fibre Li-ion structural battery electrodes, Multifunct. Mater. 1 (1) (2018), 015003.
[35] J. Hagberg, S. Leijonmarck, G. Lindbergh, High precision coulometry of commercial PAN-based carbon fibers as electrodes in structural batteries, J. Electrochem. Soc. 163 (8) (2016) A1790–A1797.
[36] Toray, "types of carbon fiber [Online]. Available: https://www.toraycma.com/page.php?id=661, 2020. (Accessed 30 November 2020).
[37] Teijin, "Tenax® filament yarn [Online]. Available: https://www.teijincarbon.com/products/tenaxr-carbon-fiber/tenaxr-filament-yarn, 2020. (Accessed 30 November 2020).
[38] K. Thompson, D. Lawrence, D.J. Larson, J.D. Olson, T.F. Kelly, B. Gorman, In situ site-specific specimen preparation for atom probe tomography, Ultramicroscopy 107 (2–3) (2007) 131–139.
[39] F. Liu, H.O. Andrén, Effects of laser pulsing on analysis of steels by atom probe tomography, Ultramicroscopy 111 (6) (2011) 633–641.
[40] J. Angseryd, F. Liu, H.O. Andrén, Nanostructure of a cubic BN cutting tool material, Int. J. Refract. Metals Hard Mater. 49 (1) (2015) 283–287.

[41] C. Schlueter et al., "The new dedicated HAXPES beamline P22 at PETRAIII," AIP Conf. Proc., vol. 2054, no. January 2019, 2019.
[42] M.B. Trzhaskovskaya, V.G. Yarzhemsky, "Dirac–Fock photoionization parameters for HAXPES applications, Atomic Data Nucl. Data Tables 119 (2018) 99–174.
[43] F. Vurpillot, J. Houard, A. Vella, B. Deconihout, Thermal response of a field emitter subjected to ultra-fast laser illumination, J. Phys. D Appl. Phys. 42 (12) (2009).
[44] D. Joester, A. Hillier, Y. Zhang, T.J. Prosa, Organic materials and organic/inorganic heterostructures in atom probe tomography, Micros. Today 20 (3) (2012) 26–31.
[45] A. Jablonski, C.J. Powell, Practical expressions for the mean escape depth, the information depth, and the effective attenuation length in Auger-electron spectroscopy and x-ray photoelectron spectroscopy, J. Vac. Sci. Technol. A Vacuum, Surfaces, Film. 27 (2) (2009) 253–261.
[46] S. Tanuma, C.J. Powell, D.R. Penn, Calculations of electron inelastic mean free paths. IX. Data for 41 elemental solids over the 50 eV to 30 keV range, Surf. Interface Anal. 43 (3) (2011) 689–713.
[47] J.T. Titantah, D. Lamoen, Carbon and nitrogen 1s energy levels in amorphous carbon nitride systems: XPS interpretation using first-principles, Diam. Relat. Mater. 16 (3) (2007) 581–588.
[48] T. Sharifi, G. Hu, X. Jia, T. Wågberg, Formation of active sites for oxygen reduction reactions by transformation of nitrogen functionalities in nitrogen-doped carbon nanotubes, ACS Nano 6 (10) (2012) 8904–8912.
[49] M. Scardamaglia, et al., Spectroscopic observation of oxygen dissociation on nitrogen-doped graphene, Sci. Rep. 7 (1) (2017) 1–11.
[50] K. Artyushkova, Misconceptions in interpretation of nitrogen chemistry from x-ray photoelectron spectra, J. Vac. Sci. Technol., A 38 (3) (2020), 031002.